Rare Met. (2021) 40(3):616–625
https://doi.org/10.1007/s12598-020-01513-2

RARE METALS
www.editorialmanager.com/rmet

ORIGINAL ARTICLE

Oxidation behavior of Ni-based superalloy GH738 in static air between 800 and 1000 °C

Jue Wang*, Hao Xue, Ying Wang

Received: 21 August 2019 / Revised: 16 October 2019 / Accepted: 28 June 2020 / Published online: 5 August 2020

Abstract The oxidation behavior of a nickel-based superalloy GH738 was studied by isothermal oxidation tests in still air at different temperatures, with exposure time up to 100 h. Oxidation-kinetic curves were plotted using the mass gain method. The surface and cross-sectional morphologies were observed by scanning electron microscopy (SEM). A composition analysis and an oxidation-product identification were conducted using energy-dispersive X-ray spectroscopy (EDS) and an X-ray diffraction (XRD), respectively. The results showed that GH738 exhibited parabolic oxidation-kinetic curves, with stable parabolic-rate constants at each temperatures. The activation energy of oxide growth was calculated to be 329.6 kJ·mol^{-1}. Cr_2O_3 (chromia) was the external oxidation product at 800 °C. A TiO_2–Cr_2O_3 double-layer structure was formed at 900 °C. The position of TiO_2 changed from the oxide–metal interface to the air–oxide interface by the diffusion of Ti atoms in chromia during the oxidation time at this temperature. Spallation was observed in the $Cr_{0.12}Ti_{0.78}O_{1.74}$–$Cr_2O_3$ multi-layer oxide of at 1000 °C, which increased the oxidation rate. For all the tests, the main internal oxide was always Al_2O_3. The entire GH738 oxidation process was interpreted by the competitive diffusion of elements (Cr, Ti, Ni, etc.) in metal matrix and chromia, while a schematic diagram of oxidation process was proposed.

J. Wang*
Jiangsu Key Laboratory of Advanced Structural Materials and Application Technology, Nanjing 211167, China
e-mail: jue_wang@njit.edu.cn

J. Wang, H. Xue, Y. Wang
School of Materials Science and Engineering, Nanjing Institute of Technology, Nanjing 211167, China

Keywords GH738; Oxidation behavior; Diffusion; Multi-layer structure

1 Introduction

GH738 is a nickel-based superalloy widely used to manufacture turbines and blades in aircraft engines and power systems because of its excellent strength-toughness combination and corrosion resistance at elevated temperatures. The mechanical properties of this nickel-based superalloy are ascribed to the high-temperature stability of strengthening phases (e.g., γ', carbides) and fcc matrix. The high Cr content provides the resistance to flue gas by forming a protective Cr_2O_3 oxide layer [1, 2]. Many studies have been focused on the high-temperature mechanical properties of GH738, e.g., creep [3, 4], fatigue crack-growth behaviors and structural stability [5–8]. Another research series have investigated the deformation mechanisms and process optimization of hot and cold workings [9–12].

In contrast, few oxidation behavior reports are available for this alloy. Chen et al. [13] studied the Waspaloy oxidation process at 750 and 1000 °C, analyzing the types and morphologies of oxidation products. Pike and Srivastava [14] focused on the depth of internal oxidation in flowing air or dynamic oxidation tests. However, some details regarding the oxidation behavior of this alloy are still lacking. The influence of oxidation temperature on the elemental-diffusion behavior and oxide species is not clear. The model diagram of oxidation behavior for GH738 is not constructed. The existence of some oxidation products is still controversial.

The oxidation behavior of high-temperature alloys has been researched extensively [15–29]. The characteristics can be summarized as follows.

1. *Diffusion control* The development of oxide scales on superalloys is controlled by the transportation of O and alloy elements. Therefore, the oxidation-kinetic curves follow a parabolic-rate law during the thickening stage of oxide scale [15–19].
2. *Selective oxidation* The oxide-layer formation of a specific element depends on both its activity and content. Cr_2O_3 (chromia) and Al_2O_3 (alumina) are the most common oxides in the external and internal oxide layers, respectively, for superalloy with high Cr/Al ratio [20, 21]. In contrast, when Al content is higher than 3 wt%, alumina appears in the external oxide layer [22]. In addition, Ti, Mn, Ni and Fe oxides can also be found in the oxidation process [16, 21, 30].
3. *Multi-layer structure* Composite oxide and multi-layer structures are frequently found in superalloys because of their high alloying degree, e.g., a $NiCr_2O_4$–Cr_2O_3–TiO_2 multi-layer in 740H [16], a NiO–$NiCr_2O_4$–Cr_2O_3 triple layer in 617, $MnCr_2O_4$–Cr_2O_3 in Haynes 230 [15], $(Cr_{0.88}Ti_{0.12})_2O_3$ and Cr_2NiO_4 in 720Li [24]. The morphology and distribution details of these oxides are determined by the compositions and test conditions (temperature and time). The formation and evolution of this multi-layer oxide directly affect the oxidation resistance of superalloys.

In this paper, the oxidation behavior of GH738 was studied by isothermal oxidation tests in still air. The surface and cross-sectional morphologies were observed by scanning electron microscopy (SEM). A composition analysis and oxidation-product identification were conducted by energy-dispersive X-ray spectroscopy (EDS) and X-ray diffraction (XRD). Oxidation-kinetic curves were plotted by the mass gain method. The diffusion behavior of elements at different temperatures and its effect on the formation of oxidation products were systematically discussed. The reason for the absence of a NiO/$NiCr_2O_4$ spinel was investigated by comparing a series of superalloys. Finally, the oxidation mechanisms of GH738 were analyzed and a schematic diagram of the oxidation process for this material was proposed.

2 Experimental

The chemical compositions of GH738 in this study are listed in Table 1. Rectangular samples with the size of 20 mm × 10 mm × 2 mm were cut from the center of a wrought bar, which was subjected to the standard heat-treatment procedure: 1020 °C/4 h solid solution + 845 °C/24 h aging + 760 °C/16 h aging. The initial grain size is about 40 μm with very fine (< 100 nm) Ni_3Al particles uniformly distributed in the gamma matrix.

Table 1 Measured chemical composition of GH738 (wt%)

C	Cr	Co	Mo	Fe	Al	Ti	Ni
0.055	19.48	12.90	3.99	0.45	1.40	2.95	Bal.

All the specimens were ground to the appropriate surface roughness (< 1 μm) and ultrasonically cleaned in acetone and ethanol, followed by hot-air drying. The oxidation experiments were carried out at 800, 900 and 1000 °C for 12, 25, 50, 75 and 100 h at each temperature in a box furnace, in the air condition of laboratory environment. After the oxidation tests, the samples were fully air cooled to room temperature and weighed, along with the spalled oxide, if any, by an electronic balance with accuracy of ± 0.1 mg. The weight change per unit area (Δm_A) was recorded by the equation:

$$\Delta m_A = \frac{m_1 - m_0}{A} \tag{1}$$

where m_1 and m_0 are the total mass of a sample and crucible after and before oxidation experiment, respectively, and A is the surface area of a single specimen.

The morphology and compositions of oxide layer were analyzed by SEM (ZEISS sigma) equipped with EDS (XFlash6160). The oxide was identified by XRD (UltimaIV) in the diffraction-angle (2θ) range of 20°–80°. The samples for cross-sectional morphology observation were ground and mechanically polished and then analyzed by elemental line scanning and mapping, combined with back-scattered electron (BSE) images.

3 Results

3.1 Oxidation kinetics

The weight changes of all samples under different oxide conditions are shown in Fig. 1a. The mass gain per unit area increases with oxidation time, while its increment decreases continuously at every temperature. Furthermore, a larger mass gain is observed at higher temperature, especially at 1000 °C. All the measured data are plotted in a Δm_A versus $t^{1/2}$ figure (Fig. 1b). A good linear relationship is found at each temperature in this coordinate system, indicating a parabolic law between the mass gain per unit area and oxidation duration, which represents a diffusion-controlled oxidation behavior [15, 16].

The parabolic-rate constants are calculated according to the following equation [16]:

$$\Delta m_A = k_p^{1/2} \cdot t^{1/2} \tag{2}$$

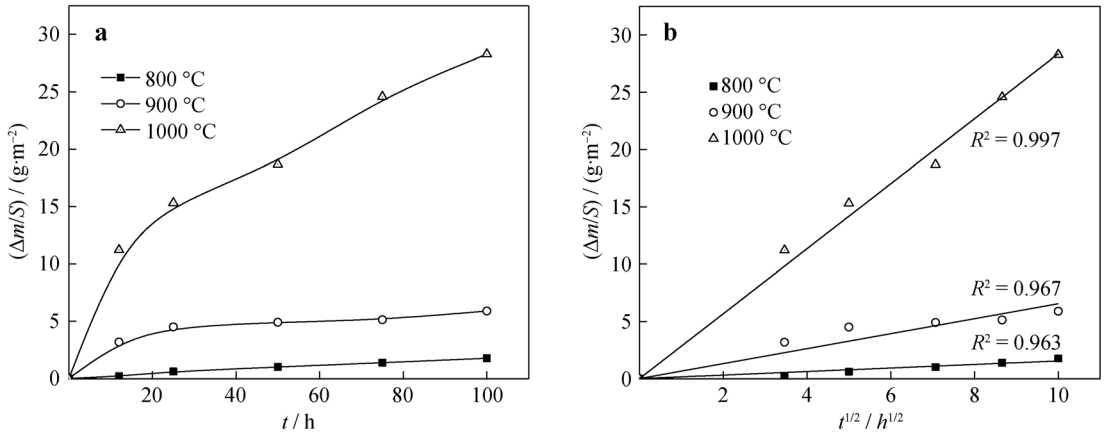

Fig. 1 Oxidation-kinetic curves of GH738 at 800-1000 °C: **a** weight change per area ($\Delta m/S$) versus oxidation time (t); **b** weight change per area ($\Delta m/S$) versus $t^{1/2}$

where k_p is the parabolic-rate constant, and t is the oxidation time. The values are listed in Table 2 as well as the adjusted coefficient of determination (adj. R^2). This shows that the parabolic-rate constants for GH738 increases with temperature. These values are in the range of 1×10^{-14}–1×10^{-10} $g^2 \cdot cm^{-4} \cdot s^{-1}$ which are comparable to the data in Ref. [13] and other superalloys of chromia former, e.g., 8.8×10^{-13} $g^2 \cdot cm^{-4} \cdot s^{-1}$ at 900 °C for Alloy 617, 3.8×10^{-13} $g^2 \cdot cm^{-4} \cdot s^{-1}$ at 900 °C for Haynes 230 [15], 1.0×10^{-13}/2.4×10^{-13}/46.2×10^{-13} $g^2 \cdot cm^{-4} \cdot s^{-1}$ at 800/900/1000 °C for Haynes 282 [17], 417×10^{-13}/833×10^{-13}/1720×10^{-13} $g^2 \cdot cm^{-4} \cdot s^{-1}$ at 1050/1110/1170 °C for Alloy 740H [16].

3.2 Identification of oxide products

XRD patterns of GH738 oxidized at different temperatures for 12 and 100 h are shown in Fig. 2. It can be seen that temperature affects the type of oxidation product, while the exposure time mainly influences the relative peak strength. The matrix and Cr_2O_3 are detected at 800 °C (Fig. 2a). As oxidation progressed, the intensities of the matrix peaks reduced significantly, indicating the gradual coverage and thickening of oxide layers.

The peaks of another oxide, TiO_2, appear at the oxidation temperature of 900 °C (Fig. 2b). Similarly, the peak intensities of matrix and oxides change oppositely from 12 to 100 h. Compared to XRD patterns of 900 °C, the main products of Cr_2O_3 and a complex oxide, $Cr_{0.12}Ti_{0.78}O_{1.74}$, are detected at 1000 °C (Fig. 2c). It should be noted that matrix can hardly be found in the 1000 °C/100 h condition, which means a considerably thick oxide layer on the sample surface.

Table 2 Oxidation parabolic constants and adj. R^2 at different temperatures

Temperature/°C	k_p/(10^{-13} $g^2 \cdot cm^{-4} \cdot s^{-1}$)	Adj. R^2
800	0.664	0.963
900	12.000	0.967
1000	223.600	0.997

3.3 Morphology and composition analysis of oxide scale

The typical morphologies of GH738 oxidized at 800 and 900 °C are shown in Fig. 3. A uniform oxide scale is observed on the sample surface at 800 °C/12 h. The grains and grain boundaries are not easily resolved under this condition, which indicates the formation of a not-very-thin oxide layer (Fig. 3a). However, the sample surface, which is covered by oxide particles, is considerably rugged and uncompact in the high-magnification figure (Fig. 3b). These particles coarsen and aggregate at 800 °C/100 h, increasing the density and flatness of the oxide surface (Fig. 3c).

Numerous evenly distributed oxide nodules are found in the condition of 900 °C/12 h (Fig. 3d), composing a more coarsened structure compared to the morphology at 800 °C. These nodules are formed by the coalescence of small particles, which can be concluded by Fig. 3e. When the oxidation time proceeds to 100 h, the morphology of oxide transforms from discrete islands (large nodules) to consecutive agglomerations (Fig. 3f), leading to a further improvement in the oxide density. It is worth noting that no apparent spallation of oxide layer is apparent at 800 and 900 °C. This indicates a strong adhesion between the scale and matrix, as well as the presence of low stresses inside the oxide layer.

EDS analysis, which applies complementary information to XRD results, was carried out to quantify the oxide

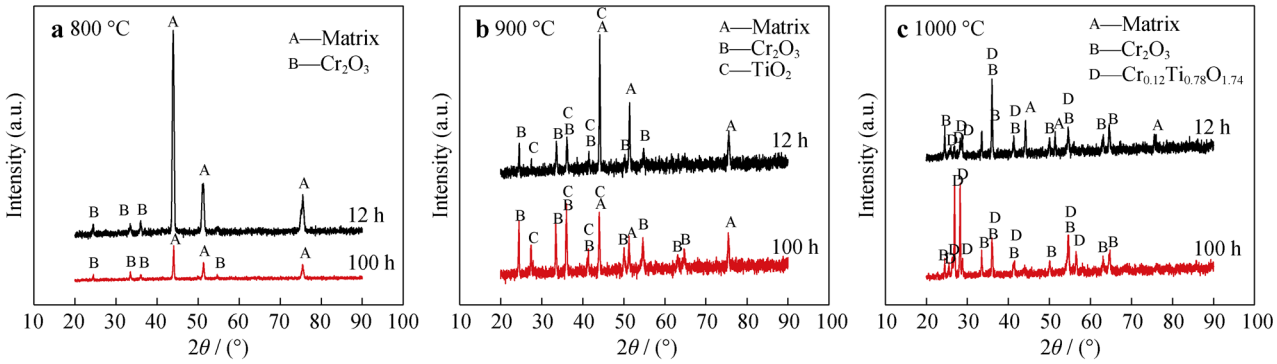

Fig. 2 XRD patterns of GH738 oxidized for 12 and 100 h: **a** 800 °C, **b** 900 °C, and **c** 1000 °C

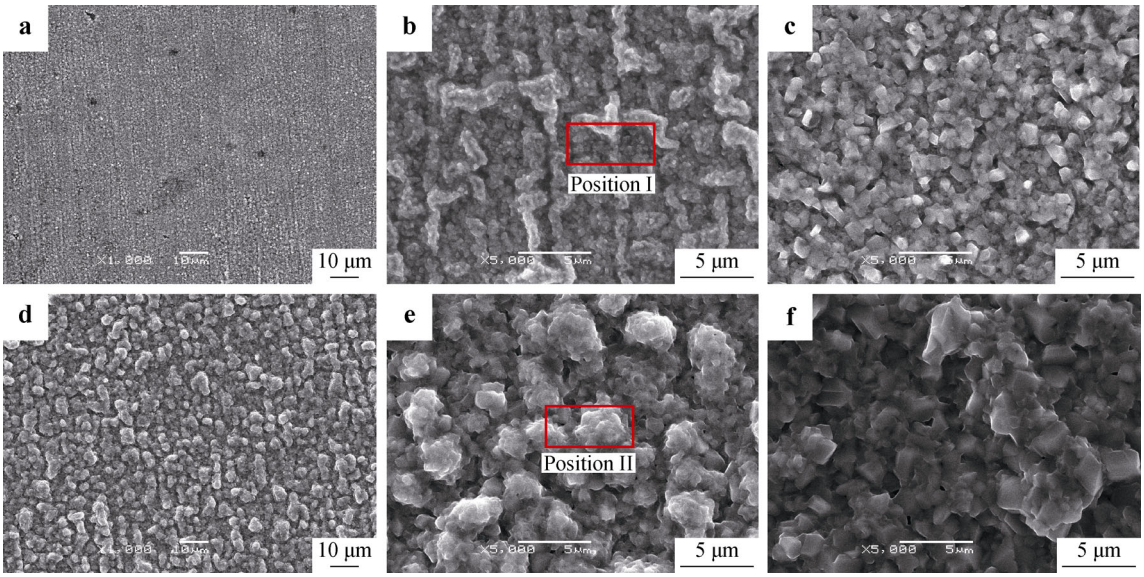

Fig. 3 SEM images of oxides in sample surface for GH738, oxidized at 800 and 900 °C: **a**, **b** 800 °C/12 h; **c** 800 °C/100 h; **d**, **e** 900 °C/12 h; **f** 900 °C/100 h

compositions. The surface compositions of GH738, after oxidation tests at 800 and 900 °C for 12 h, are listed in Table 3. Compared to the alloy compositions, O and Cr contents are much higher at 800 °C/12 h (Position I in Fig. 3b), while the changes of other elements are relatively small. This corresponds to the formation of a Cr_2O_3 oxide layer with limited thickness.

When the oxide condition is 900 °C/12 h, the O, Cr and Ti contents on the sample surface increase significantly (Position II in Fig. 3e), which is consistent with the appearance of TiO_2 and Cr_2O_3 in the XRD results. The low content of other elements on the surface of this sample indicates the thickening of the oxide layer. The two oxides will be distinguished by cross-sectional analysis later.

Table 3 Compositions of oxides in Fig. 3 after oxidation tests at 800 and 900 °C for 12 h (wt%)

Oxide	O	Cr	Co	Mo	Al	Ti	Ni
Position I	8.21	33.01	9.25	3.52	2.14	4.20	39.67
Position II	12.91	65.02	1.34	0.55	1.03	15.49	3.66

Figure 4 shows the surface morphology of GH738 samples after oxidation at 1000 °C. The spallation of oxide layer is quite obvious at 1000 °C/12 h, leading to a complex surface structure (Fig. 4a). Three regions with different morphologies can be identified by SEM and EDS (Table 4). Region I: large Cr-rich oxide nodules are observed in this area, which is similar to the sample with the 900-°C-oxidation tests (Fig. 3d). Cr_2O_3 is considered to be the main oxidation products by XRD analysis. Region II: the oxide in this area possesses a regular grain shape (higher magnification in Fig. 4b), containing fairly high Cr (41.21 wt%) and Ti (43.09 wt%) contents. According to XRD results, it may be a mixed oxide of $Cr_{0.12}Ti_{0.78}O_{1.74}$ and Cr_2O_3. Region III: this area is the secondary oxide layer after spallation. The compact structure and high content of Cr (81.51 wt%) indicate the Cr_2O_3 oxide

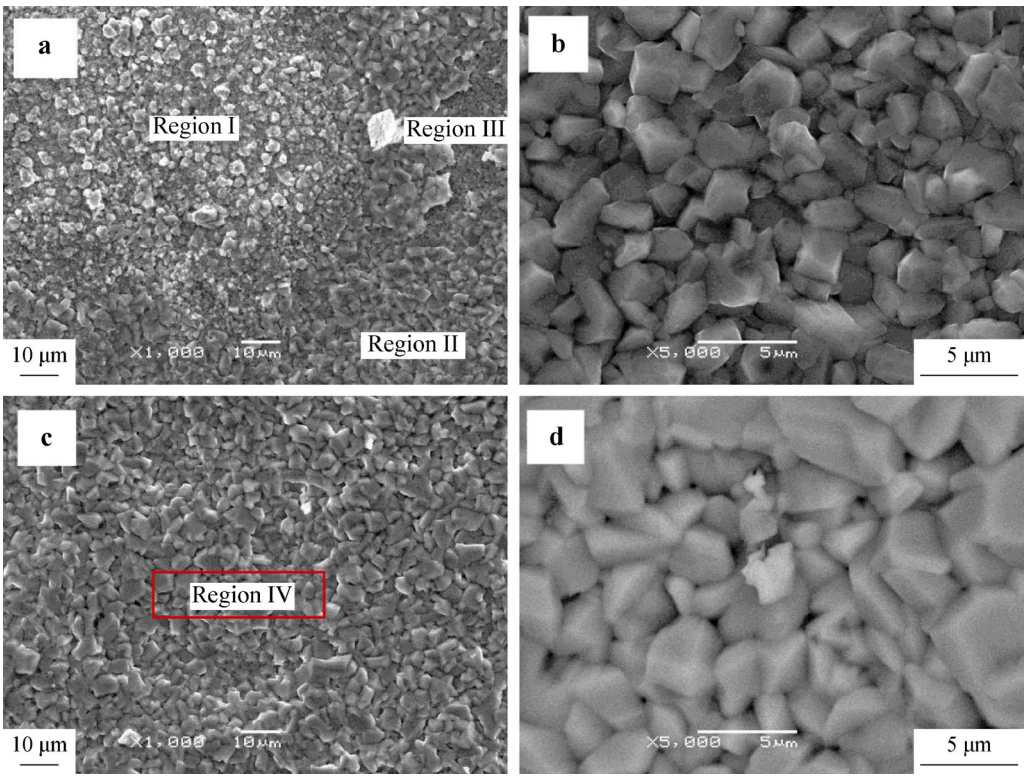

Fig. 4 SEM images of oxides in sample surface for GH738, oxidized at 1000 °C: **a** 12 h; **b** magnification of Region II; **c** 100 h; **d** BSE magnification of Region IV

Table 4 Compositions of oxides in Fig. 4 after tests at 1000 °C for 12 and 100 h (wt%)

Oxide	O	Cr	Co	Mo	Al	Ti	Ni
Region I (12 h)	9.60	54.53	17.80	0.43	0.46	6.87	10.31
Region II (12 h)	12.07	41.21	1.52	0.24	0.30	43.09	1.56
Region III (12 h)	10.43	81.51	0.54	0.52	0.41	4.74	1.84
Region IV (100 h)	13.88	12.79	–	0.69	0.12	72.10	0.41

product. As the oxidation time extends to 100 h, the areas with oxide nodules disappear, while the proportion of "grain shape" areas increases significantly. Compared to the compositions of this kind of region at 1000 °C/12 h, Ti content improves to 72.1 wt%. Combining the results of BSE image (Fig. 4d) and XRD patterns, the dominant oxide is $Cr_{0.12}Ti_{0.78}O_{1.74}$. It should be noted that small voids exist among the oxide bulks, meaning that the density of external oxide layer is low at 1000 °C.

3.4 Cross-sectional morphologies characterization

A cross-sectional analysis was carried out to investigate the details of internal and external oxides, especially the changes in layer structure, morphology and compositions along the depth direction. The typical cross-sectional morphology of GH738 samples after 1000 °C/100 h oxidation is shown in Fig. 5a. The internal and external oxidation areas can be easily distinguished by the oxide/metal substrate interface. In the former area, oxides are discrete or semi-continuous, some of which extend along the grain boundary into the metal matrix up to about 44 μm. The external oxidation area possesses a complex multi-layer structure. It contains a light-gray layer near the oxide/metal substrate interface and a dark-gray layer near the oxide/air interface in the BSE figure (Fig. 5a, b), with a total thickness of about 17 μm.

A line scanning analysis of the blue line in Fig. 5b was conducted to study the oxide compositions in the direction perpendicular to the interface (Fig. 5c). Three parts with different composition characteristics can be identified. Part I: the outermost oxide layer (corresponding to the dark-gray area in Fig. 5b) is rich in Ti and O, also containing a certain amount of Cr. Combining the XRD and surface-analysis results, this layer is determined to be $Cr_{0.12}Ti_{0.78}O_{1.74}$. The thickest area of this layer is about 5.8 μm. Part II: the light-gray layer, which is just beneath the $Cr_{0.12}Ti_{0.78}O_{1.74}$ oxide, contains massive amounts of Cr and O, instead of Ti. This layer can be identified as Cr_2O_3, according to the composition and spallation analysis noted

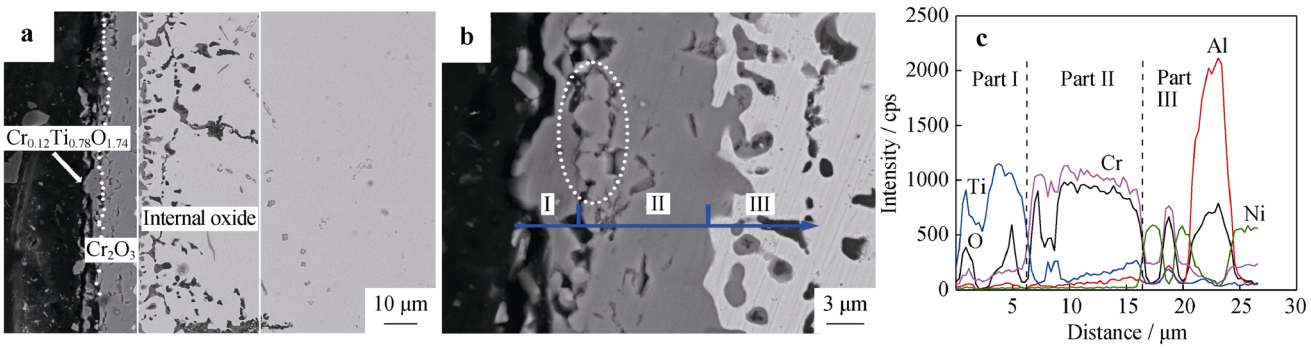

Fig. 5 Cross-sectional SEM images and line scanning results of GH738, oxidized at 1000 °C/100 h: **a** typical cross-sectional morphology; **b** magnification of **a** and **c** line scanning results

above. Part III: the decrease of O content and increase of Ni content indicates the approaching of oxide/metal substrate, while the high Al content at the 20-μm depth indicates the appearance of the internal oxide.

A further analysis of the external oxidation morphology shows that a large number of protuberances and fractures exist near the interface between the $Cr_{0.12}Ti_{0.78}O_{1.74}$ layer and the Cr_2O_3 layer (circled in Fig. 5b). These defects are related to the difference in thermal-expansion coefficients between the two layers [15]. The cracks are caused by the stress during the heating and cooling treatments, while the poor adhesion between the two layers aggravates their formation.

It is reported that these defects increase the oxidation rate by accelerating the permeation of oxygen atoms into the matrix [15, 16]. It is noteworthy that Ti content keeps a low value from the interface between $Cr_{0.12}Ti_{0.78}O_{1.74}$/$Cr_2O_3$ layer to the internal oxidation area, which indicates its outward diffusion.

The cross-sectional morphologies and line scanning results (along the blue lines) of GH738 after 900 °C/25 h and 900 °C/50 h oxidation are shown in Fig. 6. Although XRD peaks show the same oxidation products of Cr_2O_3 and TiO_2 in these two conditions, the oxide-layer structure and the elemental distribution are obviously influenced by the holding time. In the test condition of 900 °C/25 h, similar Cr and Ti contents are detected in the outermost layer (under the interface between air and oxide) (Fig. 6b). However, Cr content increases significantly just below this very thin layer (< 1 μm). This Cr-rich layer is about 2 μm in thickness.

A Ti–rich zone is observed between the outer and inner-oxidation areas (near the interface between oxide/metal), which appears as a 0.5-μm-thick dark-gray layer in BSE figures. This "mixed Cr/Ti—Cr-rich—Ti-rich" structure is also observed also in IN939 superalloy [20]. The internal oxide product is still Al_2O_3 which extends to 9 μm along the grain boundary.

When the oxide holding time prolongs to 50 h, the thickness of the inner and outer oxide layers increases to 6.0 and 13.8 μm, respectively (Fig. 6c). Compared to the samples of 900 °C/25 h, Ti content is much higher than Cr content near the oxide/air interface. The depth of this dark-gray layer is about 1.5 μm in the BSE figure. The secondary layer in the external oxidation area is still rich in Cr, which is 4.5 μm in thickness (Fig. 6c, d). It is worth noting that the Ti-rich layer near the oxide/metal interface at 900 °C/25 h disappears when the holding time extends to 50 h. In addition, the internal oxide products contain more Ti than those in the short-time oxidation.

Considering the high content of Ti on the sample surface, a transport process of this element can be deduced. During the holding time, Ti atoms diffuse from oxide/metal interface at the early oxidation stage to the air/oxide interface. As these atoms are transported to the surface, a new group of Ti atoms diffuse from metal matrix to the interface between inner and outer oxidation areas. Grain boundaries may provide a short-circuit diffusion path in this process, which leads to the intergranular inner-oxidation features in the depths of the matrix.

Another difference between the 50- and 25-h samples is the appearance of fractures and protuberances. This is similar to the morphology of oxidized samples at 1000 °C. It can be attributed to the development of the multi-layer structures.

4 Discussion

4.1 Elemental-diffusion behavior and oxidation mechanism for GH738

GH738 possesses parabolic oxidation-kinetic curves in the temperature range of 800–1000 °C, which indicates the essential role of elemental diffusion. Furthermore, the parabolic-rate constant at each temperature remains invariant during the holding time. This phenomenon means that the diffusion element which controls the oxidation rates is less influenced by oxidation time under the

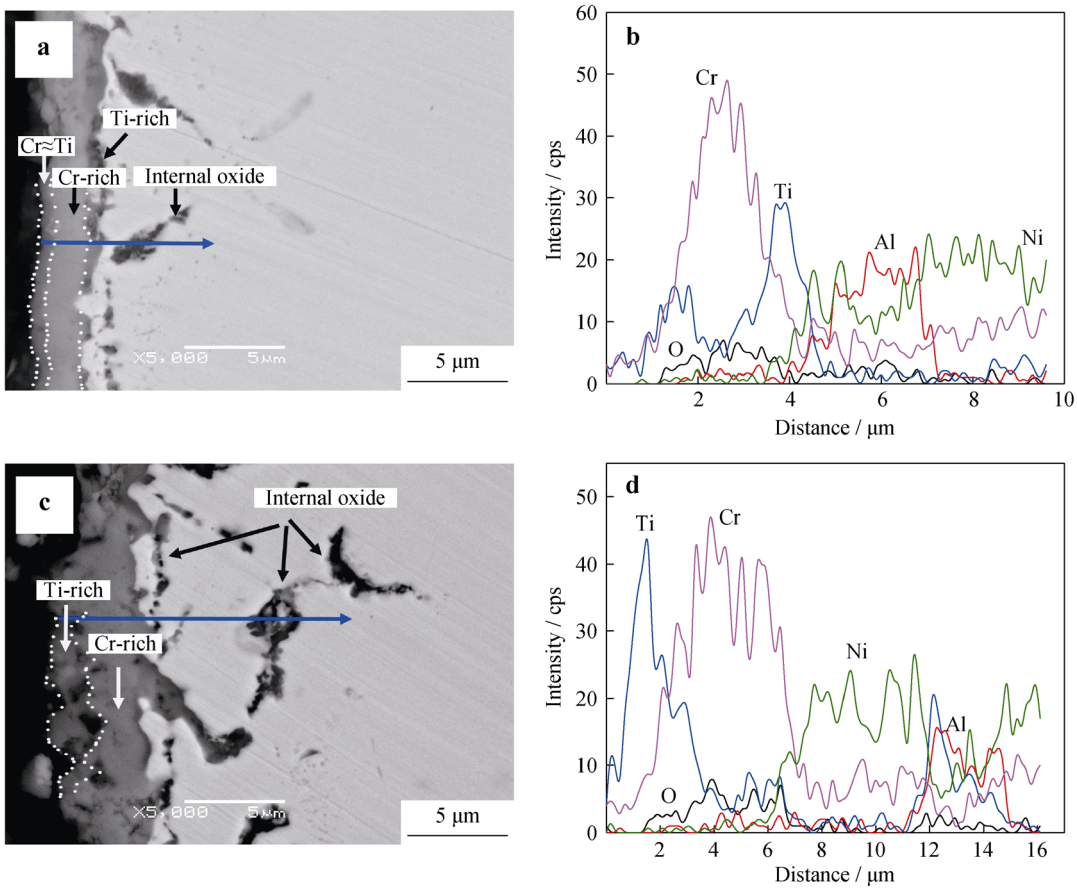

Fig. 6 Cross-sectional SEM images and line scanning results (blue lines) of GH738 oxidized at **a**, **b** 900 °C/25 h and **c**, **d** 900 °C/50 h

experimental conditions [15, 17, 31]. The elemental-diffusion behavior at different test temperatures is analyzed as follows. According to the test results of XRD and SEM, the external oxidation products at 800 °C are deduced to be Cr_2O_3. Therefore, the diffusion of Cr in the chromia layer determines the development of this oxide. It is reported that the diffusion rate of Cr in chromia is relatively low [32–34], which corresponds to the low parabolic-rate constant at this temperature.

It should be noted that the free energies of formation for the most stable oxides of Ti and Cr are − 440 and − 293 kcal·kJ·mol^{-1} [35], respectively. Although Ti is more thermodynamically favored, its oxide is not observed at the temperature of 800 °C (Fig. 7a). Jiang et al. [16] attributes the selective oxidation of Cr_2O_3 to the high Cr/Ti ratio and low content of Ti.

The parabolic-rate constant increases from 0.664×10^{-13} to 12×10^{-13} g^2·cm^{-4}·s^{-1}) at the oxidation temperature of 900 °C. It can be primarily interpreted by the acceleration of elements diffusion at high temperature. An obvious difference between the oxides at 800 and 900 °C is the observation of TiO_2, which appears on the interface of both air/oxide and oxide/metal substrate in the condition of 900 °C/25 h. In contrast, when the oxidation time extends to 50 h, the latter Ti-rich area disappears, leaving only the former one with higher Ti content. Since Cr_2O_3 exists in the secondary outer layer of oxide throughout the oxidation time, the outward-transportation process of the Ti atoms through the chromia to the sample surface is another core factor for the oxidation of 900 °C. At this oxidation temperature, Ti atoms obtain sufficient energy to diffuse in metal matrix, which results in the formation of Ti oxide. However, the diffusivity of Ti in Cr_2O_3 is lower than that in the matrix. It causes the accumulation of Ti atoms just below the external oxide layer (Cr_2O_3) in short-time oxidation process, which leads to the formation of Ti-rich zone between the oxide layer and metal matrix (Fig. 7b). With the prolongation of oxidation time, Ti atoms diffuse from the interface of oxide/metal to external oxide, leading to the disappearance of Ti-rich zone at 900 °C/50 h and 900 °C/100 h. With the appearance of TiO_2, the thermal-expansion property differences between TiO_2 and Cr_2O_3 lead to the formation of fractures in the external oxide layer, which accelerates the penetration of O into the metal. This is another reason for the high oxidation rate at 900 °C.

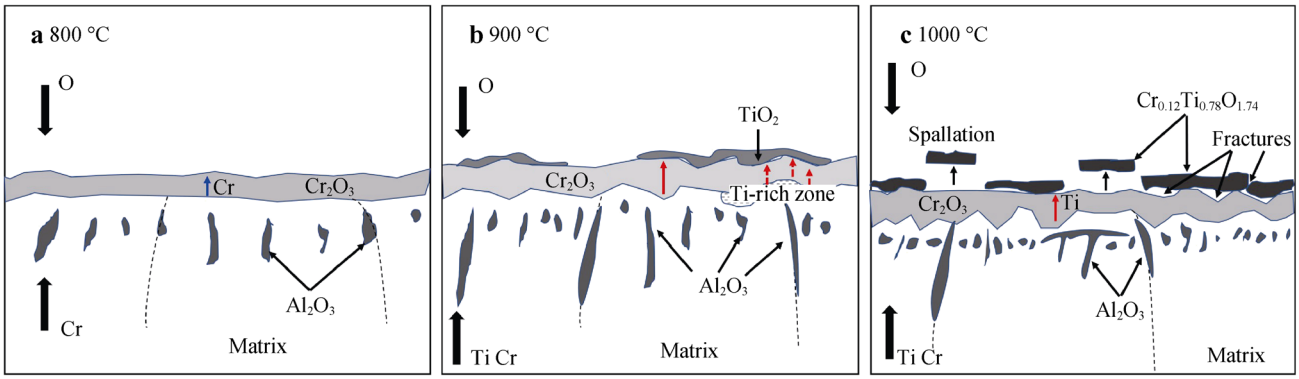

Fig. 7 Schematic diagrams of oxidation mechanism for GH738 at **a** 800 °C, **b** 900 °C, and **c** 1000 °C

The largest parabolic-rate constant (i.e., the highest oxidation speed) is obtained at 1000 °C for GH738. A composite oxide of $Cr_{0.12}Ti_{0.78}O_{1.74}$ forms on the sample surface. This oxide spalls easily and contains a number of fractures and voids, which promotes the oxidation. A dense layer of Cr_2O_3 is located just below this composite scale. No Ti-rich area is found near the interface of oxide/metal at 1000 °C/12 h, which is similar to the long-time oxidation samples at 900 °C. Considering the diffusion of both Ti and Cr atoms in the existing Cr_2O_3 oxide layer, as well as the content of Ti higher than that of Cr in $Cr_{0.12}Ti_{0.78}O_{1.74}$, Ti ions diffuse much more easily through chromia at this temperature.

The main internal oxidation product is Al_2O_3 for all the tests, with the appearance of TiO_2 at 900 °C. The morphology, distribution and compositions of the internal oxide are similar to other superalloys with a high Cr/Al ratio [16, 20, 36], which is difficult to form Al_2O_3 in the external oxide layer. The diffusion of Al atoms from the matrix to the metal–oxide interface, especially the rapid diffusion along the grain boundaries, is the main elemental-diffusion mode of the internal oxidation. The schematic diagrams of oxidation mechanism for GH738 are shown in Fig. 7.

The activation energy for oxide growth can be calculated by plotting different k_p in the form of Arrhenius equation:

$$k_p = k_0 \exp\left(\frac{-Q_{ox}}{RT}\right) \tag{3}$$

where Q_{ox} is the activation energy, R is gas constant, T is the exposure temperature and k_0 is a constant. The graph shows a remarkable straight line, giving the energy value of 329.6 kJ·mol^{-1} by multiplying R and fitting slope (Fig. 8). Then the mass gain equation can be expressed as:

$$(\Delta m_A)^2 = k_0 \exp\left(\frac{-329.6}{RT}\right) t \tag{4}$$

The calculated activation energy of oxide growth for GH738 is obviously higher than the diffusion activation energy of Cr ions in Cr_2O_3 (255 kJ·mol^{-1}) [13], which demonstrates the multi-elemental-diffusion behavior from another aspect. The weight gain in oxidation test in this study is due to the formation of Cr_2O_3, TiO_2, $Cr_{0.12}Ti_{0.78}O_{1.74}$ and Al_2O_3. The growth rate of each oxide obeys parabolic kinetics, resulting in the overall parabolic oxidation kinetics for GH738. However, the activation energy of all these diffusion processes, e.g., element diffusion from the matrix to the oxide–metal interface or inside the oxide, is quite different. Although the diffusion of Ti in chromia is faster than that of Cr, the lower growth rate of alumina during internal oxidation and the formation of composite oxide $Cr_{0.12}Ti_{0.78}O_{1.74}$ can both increase the activation energy of oxide growth for GH738.

4.2 Absence of NiO and $NiCr_2O_4$

A remarkable result of the current tests is the absence of nickel oxide (NiO) or $NiCr_2O_4$ spinel, which is different from the study by Chen et al. [13]. These two kinds of oxide are reported to exist in some superalloys but not all. Generally, NiO appears on the air/oxide interface, i.e., the

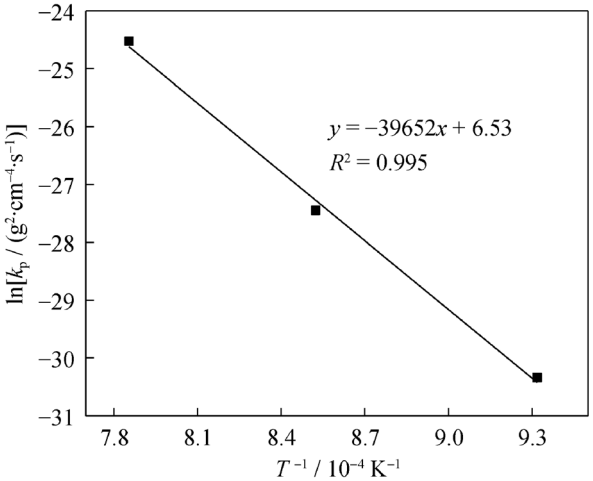

Fig. 8 Linear fit of lnk_p and 1/T of GH738 in oxidation tests

outmost layer. $NiCr_2O_4$, which is the reaction product of NiO and Cr_2O_3, is located just below the outer layer. This oxide structure is caused by the abundant supply of Ni ions for the superalloy, as well as the higher diffusion speed of Ni in chromia [34], which leads to the competitive advantage of the NiO layer growth over the Cr_2O_3 on the existing chromia. As the NiO layer has a poor density, the mass gain in oxidation test is promoted when this layer exists on the surface [16, 21].

Table 5 shows the critical elements contents of some polycrystal superalloys with or without NiO/$NiCr_2O_4$ during oxidation, as well as the corresponding test conditions [15–17, 20, 21, 23, 24, 32, 36, 37]. It is evident that these oxides do not appear in Types I and II alloys. The external oxidation products of Type I alloy are mainly rich in Ti or a Ti/Cr composite, while the surface oxide of Type II alloy is $CrMn_2O_4$ spinel [15, 32].

The composition feature of these alloys is the high content of Ti (Type I) or Mn (Type II). As the diffusivity of Mn is remarkably higher than those of Cr and Ni in chromia [34], an effective Mn-oxide layer can form on the sample surface when the amount of ions is sufficient. Unfortunately, the diffusion coefficient of Ti in chromia is not found. However, the formation of a Ti-rich oxide layer in GH738 proves that Ti with smaller ionic radii is more capable of growing on the Cr_2O_3 layer than Ni and Cr. Therefore, the forming of NiO layer by the diffusion of Ni ions in chromia is easier when other competition elements are not adequate in high Cr content superalloys. For examples, NiO/$NiCr_2O_4$ oxides are observed in the third type of alloys in Table 5 with both low contents of Ti and Mn.

Another factor in the appearance of NiO/$NiCr_2O_4$ is the oxidation time. It is doubtful whether the lack of competitive elements in the matrix will lead to the appearance of NiO/$NiCr_2O_4$, when the oxidation time is very long for Type I and II alloys. It should be noted that NiO appears in Type IV alloys which possess fairly high Ti content. This type of alloys includes the difficult-to-deform superalloy (720Li) and cast superalloys. The composition feature of these superalloys is the high content of Al, which leads to a change of external oxide from Cr-rich to Cr/Al composite or Al-rich [20]. The diffusivity differences of Ti and Ni ions in alumina and chromia may be the main reason for the formation of NiO in this type of superalloys. This study is now ongoing.

5 Conclusion

The oxidation behavior of Ni-base superalloy GH738 was studied by isothermal oxidation tests in still air at different temperatures, with exposure time up to 100 h. The GH738 alloy exhibited parabolic oxidation-kinetic curves in the tests, with stable parabolic-rate constants of 0.664×10^{-13}, 12×10^{-13}, 223.6×10^{-13} $g^2 \cdot cm^{-4} \cdot s^{-1}$ at 800, 900 and 1000 °C, respectively. The activation energy of oxide growth for GH738 was calculated to be 329.6 $kJ \cdot mol^{-1}$ by plotting different k_p in the form of Arrhenius equation. The oxidation process was controlled by the competitive diffusion of elements through the metal matrix and chromia. The external oxide was Cr_2O_3, TiO_2/Cr_2O_3, $Cr_{0.12}Ti_{0.78}O_{1.74}$/$Cr_2O_3$ at the temperatures of 800, 900 and 1000 °C, respectively. As the oxidation time increased, TiO_2 transferred from the matrix–oxide interface to the oxide–air interface by the diffusion of Ti atoms in the Cr_2O_3 at 900 °C. NiO or $NiCr_2O_4$ spinel were not observed in this study because of the high Ti content in

Table 5 Comparison of different superalloys with or without NiO/$NiCr_2O_4$ during oxidation

Types	Alloys	Content/wt%				Existence of $NiCr_2O_4$/NiO	Test temperature/°C	Refs.
		Ti	Al	Mn	Cr			
I	Haynes 282	2.55	1.70	0.30	19.0	×	800–1000	[17]
	Waspaloy	2.95	1.40	–	19.48	×	800–1000	–
II	Haynes 230	0.01	0.38	0.51	21.85	×	900/1100	[15]
	IN625	0.40	0.40	0.50	22.0	×	900/1000	[36]
	IN718	0.90	0.60	0.35	19.0	×	750–950	[23]
	Alloy A	0.36	1.34	0.29	21.9	×	930	[32]
III	617	0.38	1.10	0.04	21.8	√	900	[15]
	740H	1.66	1.40	–	25.1	√	1100/1170	[16]
	Hastelloy C4	0.24	–	0.13	15.6	√	1200	[21]
IV	K444	4.40	3.10	–	15.3	√	800/850	[37]
	IN738 LC	3.41	3.43	0.20	16.0	√	900/1100	[20]
	IN939	3.80	1.40	–	22.0	√	1100 (spalled scale)	[20]
	720Li	5.30	2.50	–	15.9	√	650/750	[24]

GH738, which was more competitive than Ni during the diffusion process in chromia. The main internal oxidation product was Al_2O_3 for all the tests, with the appearance of TiO_2 oxidized at 900 °C for 50 h.

Acknowledgments This study was financially supported by the Scientific Research Fund of Nanjing Institute of Technology (No. CKJA201802) and the Opening Project of Jiangsu Key Laboratory of Advanced Structural Materials and Application Technology (No. ASMA201802).

References

[1] Whelchel RL, Kelekanjeri VSKG, Gerhardt RA, Ilavsky J. Effect of aging treatment on the microstructure and resistivity of a nickel-base superalloy. Metall Mater Trans A. 2011;42(5):1362.
[2] Kelekanjeri VSKG, Gerhardt RA. Characterization of microstructural fluctuations in Waspaloy exposed to 760 °C for times up to 2500 h. Electrochim Acta. 2006;51(8):1873.
[3] Hyde TH, Xia L, Becker AA. Prediction of creep failure in aeroengine materials under multi-axial stress states. Int J Mech Sci. 1996;38(4):385.
[4] Sinha NK, Terada T, Au P. Minimum creep rate from primary creep using strain relaxation and recovery test. Scr Mater. 2003;49(12):1145.
[5] Liu X, Kang B, Chang K-M. The effect of hold-time on fatigue crack growth behaviors of WASPALOY alloy at elevated temperature. Mater Sci Eng A. 2003;340(1):8.
[6] Byrne J, Hall R, Grabowski L. Elevated temperature fatigue crack growth under dwell conditions in Waspaloy. Int J Fatigue. 1997;19(5):359.
[7] Goswami T. Low cycle fatigue—dwell effects and damage mechanisms. Int J Fatigue. 1999;21(1):55.
[8] Yao Z, Zhang M, Dong J. Stress rupture fracture model and microstructure evolution for Waspaloy. Metall Mater Trans A. 2013;44(7):3084.
[9] Semiatin SL, Weaver DS, Kramb RC, Fagin PN, Glavicic MG, Goetz RL, Frey ND, Antony MM. Deformation and recrystallization behavior during hot working of a coarse-grain, nickel-base superalloy ingot material. Metall Mater Trans A. 2004;35(2):679.
[10] Weaver DS, Semiatin SL. Recrystallization and grain-growth behavior of a nickel-base superalloy during multi-hit deformation. Scr Mater. 2007;57(11):1044.
[11] Stone HJ, Holden TM, Reed RC. On the generation of microstrains during the plastic deformation of Waspaloy. Acta Mater. 1999;47(17):4435.
[12] Shen G, Semiatin SL, Shivpuri R. Modeling microstructural development during the forging of Waspaloy. Metall Mater Trans A. 1995;26(7):1795.
[13] Chen JH, Rogers PM, Little JA. Oxidation behavior of several chromia-forming commercial nickel-base superalloys. Oxid Met. 1997;47(5–6):381.
[14] Pike LM, Srivastava SK. Oxidation behavior of wrought gamma-prime strengthened alloys. Mater Sci Forum. 2008;595–598:661.
[15] Kim D, Jang C, Ryu WS. Oxidation characteristics and oxide layer evolution of Alloy 617 and Haynes 230 at 900 °C and 1100 °C. Oxid Met. 2009;71(5):271.
[16] Jiang H, Dong J, Zhang M, Zheng L, Yao Z. Oxidation behavior and mechanism of Inconel 740H alloy for advanced ultra-supercritical power plants between 1050 and 1170 °C. Oxid Met. 2015;84(1):61.
[17] Pérez-González FA, Garza-Montes-de Oca NF, Colás R. High temperature oxidation of the Haynes 282© nickel-based superalloy. Oxid Met. 2014;82(3):145.
[18] Hussain N, Shahid KA, Khan IH, Rahman S. Oxidation of high-temperature alloys (superalloys) at elevated temperatures in air: I. Oxid Met. 1994;41(3):251.
[19] Cao JD, Zhang JS, Hua YQ, Rong Z, Chen RF, Ye YX. High temperature oxidation behavior of Ni-based superalloy GH586 in air. Rare Met. 2017;36(11):878.
[20] Litz J, Rahmel A, Schorr M, Weiss J. Scale formation on the Ni-base superalloys IN 939 and IN 738 LC. Oxid Met. 1989;32(3):167.
[21] Hussain N, Qureshi AH, Shahid KA, Chughtai NA, Khalid FA. High-temperature oxidation behavior of HASTELLOY C-4 in steam. Oxid Met. 2004;61(5):355.
[22] Seal S, Kuiry SC, Bracho LA. Surface chemistry of oxide scale on IN-738LC superalloy: effect of long-term exposure in Air at 1173 K. Oxid Met. 2002;57(3):297.
[23] Al-Hatab KA, Al-Bukhaiti MA, Krupp U, Kantehm M. Cyclic oxidation behavior of IN718 superalloy in air at high temperatures. Oxid Met. 2011;75(3–4):209.
[24] Wang MQ, Qu JL, Yin TZ, Sheng JY, Deng Q, Lv XD. Study on oxidation behavior of Alloy GH4720Li at high temperatures. J Iron Steel Res. 2010;22(9):28.
[25] Pan Y, Wang S. Insight into the oxidation mechanism of $MoSi_2$: ab-initio calculations. Ceram Int. 2018;44:19538.
[26] Li SL, Qi HY, Yang XG. Oxidation-induced damage of an uncoated and coated nickel-based superalloy under simulated gas environment. Rare Met. 2018;36(3):204.
[27] Guo WJ, Zhang JX, Li JS, Lu YL, Zhou XT. Oxidation properties of Ni–^{16}Mo–^{7}Cr–^{4}Fe superalloy with different Si contents at 700 °C. Chin J Rare Metals. 2019;43(5):507.
[28] Li JS, Guo WJ, Zhang JX, Lu YL, Zhou XT. Oxidation behavior of Hastelloy N superalloy at 700 °C in air with different Mn contents. Chin J Rare Metals. 2019;43(2):157.
[29] Zhou XF, Chen G, Feng YY, Qi ZX, Wang MZ, Li P, Cheng JL. Isothermal oxidation behavior of a new Re-free nickel-base single crystal superalloy at 950 °C. Rare Met. 2017;36(8):617.
[30] Al-hatab KA, Al-bukhaiti MA, Krupp U, Kantehm M. Cyclic oxidation behavior of IN718 superalloy in air at high temperatures. Oxid Met. 2011;75(3):209.
[31] Hussain N, Shahid KA, Khan IH, Rahman S. Oxidation of high-temperature alloys (superalloys) at elevated temperatures in air. II. Oxid Met. 1995;43(3):363.
[32] Rabbani F, Ward LP, Strafford KN. A comparison of the growth kinetics and scale morphology for three superalloys at 930 °C in air and low PO_2 environments. Oxid Met. 2000;54(1–2):139.
[33] Liu FJ, Zhang MC, Dong JX, Zhang YW. High-temperature oxidation of FGH96 P/M superalloy. Acta Metall Sin. 2007;20(2):102.
[34] Lobnig RE, Schmidt HP, Hennesen K, Grabke HJ. Diffusion of cations in chromia layers grown on iron-base alloys. Oxid Met. 1992;37(1–2):81.
[35] Sigler DR. The oxidation behavior of Fe–^{20}Cr alloy foils in a synthetic exhaust-gas atmosphere. Oxid Met. 1996;46(5–6):335.
[36] N'Dah E, Hierro MP, Borrero K, Pérez FJ. Study of the cyclic oxidation resistance of superalloy IN-625: lifetime predicted by COSP-modelling program. Oxid Met. 2007;68(1–2):9.
[37] Zhang S, Wang Q, Zhao XS, Zhang CH. High temperature oxidation behavior of cast Ni-based superalloy K444. J Shenyang Univ Technol. 2010;2:136.